Chemical Science

ROYAL SOCIETY OF CHEMISTRY

EDGE ARTICLE

View Article Online
View Journal

Cite this: DOI: 10.1039/d5sc09465h

All publication charges for this article have been paid for by the Royal Society of Chemistry

Self-releasing reactive oxygen species based on the metal-to-MOF charge transfer effect boost electrochemiluminescence

Xuena Mei, Shuang Zhou,* Jing Zhang,* Mei Yan, Jinghua Yu and Yan Zhang *

Traditional luminol-based electrochemiluminescence (ECL) systems rely on hydrogen peroxide as a co-reactant, but its limited solubility restricts luminescence efficiency and detection accuracy. Herein, a core–shell spherical zinc-based metal–organic framework (Zn-MOF) leverages its metal-to-MOF charge transfer (MMCT) properties to autonomously generate reactive oxygen species (ROS). The zinc core serves as an electron reservoir, facilitating electron injection into the MOF shell *via* MMCT, enabling ROS generation without exogenous oxidants. This mechanism enhances the ECL signal of luminol-derived carbon dots (L-CDs) through ROS-mediated pathways. Integrating L-CDs with Zn-MOF creates a unique reaction environment that shortens the distance between L-CDs and ROS and stabilizes the L-CDs intermediate active species, thereby improving ECL signal strength and stability in a neutral environment. The system also incorporates the specific binding of ochratoxin A to its aptamer, releasing activated DNA to trigger CRISPR/Cas12a-mediated cleavage of single-stranded DNA (ssDNA) anchored to magnetic beads and dopamine (DA). After magnetic separation, DA-ssDNA is modified on the electrode surface to suppress the initial ECL response. This sensing platform offers a robust solution for detecting mycotoxins in complex matrices, with applications in food safety and environmental monitoring.

Received 3rd December 2025
Accepted 7th January 2026

DOI: 10.1039/d5sc09465h

rsc.li/chemical-science

Introduction

Electrochemiluminescence (ECL), recognized as a highly sensitive analytical methodology, has garnered widespread acknowledgment within the biosensing domain owing to its minimal background signal and precisely controllable luminescence properties.[1,2] Luminol is a cornerstone ECL luminophore, and it generates light through reactive oxygen species (ROS) produced *via* hydrogen peroxide (H_2O_2)-mediated oxidation.[3] To enhance the luminescence efficiency of luminol, an innovative integration strategy is to combine luminol with carbon dots, integrating the powerful molecular emission of luminol with the superior electrochemical performance of carbon dots.[4,5] Compared with free luminol, luminol-derived carbon dots (L-CDs) can exhibit higher quantum yield and light stability, which is attributed to their nanoscale confinement and enhanced electron transfer efficiency. The carbon matrix can not only prevent luminol aggregation and suppress non-radiative decay, but also provide active sites for catalytic reactions, thereby amplifying ECL intensity.[6,7] However, the existing strategies mainly depend on exogenous oxidants (H_2O_2[8] or persulfates[9]) to maintain ROS generation and enhance the ECL intensity of luminol. This not only increases the complexity of the system, but also limits its applicability in biocompatible environments, due to the lower luminous efficiency of luminol in neutral media than in alkaline environments. Therefore, exploring new strategies to enhance the ECL emission of luminol in neutral aqueous solutions is of great significance for constructing a platform that can be directly compatible with the detection of biological samples.

Currently, materials with tunable ROS-generating properties are pivotal in various applications, such as environmental remediation, tumor therapy, and sensing.[10,11] These materials primarily include photocatalytic materials (*e.g.*, TiO_2,[12,13] g-C_3N_4 [14,15]), metal-based nanozymes (*e.g.*, Fe_3O_4,[16,17] CeO_2 [18,19]), and porous framework materials (metal organic frameworks (MOFs),[20,21] covalent organic frameworks[22,23]). They respectively mediate the generation of ROS through light irradiation, simulated enzymatic catalysis, or chemical oxidation processes. However, photocatalytic materials depend on a continuous external light source,[24,25] and metal-based nanozymes need exogenous H_2O_2 [26,27] to sustain ROS release. It is inevitable that the above two strategies increase system complexity. Additionally, in dynamic aqueous environments, these materials often suffer from aggregation or passivation of active sites, resulting in reduced activity. Furthermore, under physiological or neutral aqueous conditions, their ROS production rates are significantly diminished, limiting their efficiency in biosensing applications.[28,29] In contrast, the unique structural features of framework materials enable their post-modification and offer

School of Chemistry and Chemical Engineering, University of Jinan, Jinan 250022, China. E-mail: jnzs2022@126.com; zhangjingdadi@126.com; chm_zhangyan@hotmail.com

a transformative approach for self-releasing ROS generation. Through tailored structural design and compositional optimization, these frameworks enable *in situ* and sustained ROS production, eliminating reliance on external stimuli or high-concentration oxidants. Here, a core–shell spherical zinc-based MOF (Zn-MOF) was synthesized and utilized as a self-releasing ROS material to enhance the luminescence efficiency of luminol. The intrinsic metal-to-MOF charge transfer (MMCT) characteristics of Zn-MOF enabled it to efficiently generate ROS without exogenous reagents and to remain stable in a neutral aqueous environment. Its hierarchical porous structure facilitated efficient diffusion of reactants and electron transport, enabling it to maintain high catalytic activity even at low concentrations. Additionally, integrating a luminophore within the MOF could effectively leverage its inherent structural advantages, including ordered porosity, high specific surface area, and tunable cavity dimensions.[30] Thus, by encapsulating L-CDs in the nanoconfined channels of Zn-MOF, molecular aggregation was minimized, and non-radiative transitions were suppressed due to the spatial confinement, significantly enhancing the luminescence efficiency of L-CDs. Simultaneously, the luminophore was stabilized against environmental perturbations by the rigid MOF, with both the radiative quantum yield and long-term photostability being significantly enhanced. This collaborative combination provided a robust platform for optimizing the luminescence performance in neutral aqueous environments.

In order to achieve high-precision detection of biological targets in complex sensing environments, it is crucial to select appropriate interfacial driving forces to optimize the signal transduction mechanisms of the sensing platform.[31,32] For this issue, the CRISPR/Cas12a system offers a powerful solution due to its unique trans-cleavage activity.[33] In the presence of target DNA, Cas12a indiscriminately cleaved adjacent single-stranded DNA (ssDNA), which was anchored at one end to dopamine (DA). DA-ssDNA was transferred to the electrode surface following magnetic separation, which subsequently enabled DA alter charge transfer at the sensing interface and modulate the ECL response. The core mechanism lies in DA's antioxidant capacity, wherein its phenolic hydroxyl moieties undergo redox reactions with ROS.[34,35] This interaction effectively scavenges ROS, thereby reducing their availability for reaction. Therefore, its dual role as a signal transducer and amplifier enhanced the biosensing platform's sensitivity and specificity.

Herein, a core–shell spherical Zn-MOF with self-releasing ROS properties was synthesized to improve the ECL response of the L-CDs-H_2O/O_2 system *via* ROS-mediated pathways. Within the Zn-MOF structure, the zinc core served as an electron reservoir and facilitated electron injection into the MOF shell *via* the MMCT effect. This not only enabled efficient endogenous ROS generation but also eliminated interference from exogenous reagents. In addition, the irregular surface microstructure of Zn-MOF was leveraged to encapsulate L-CDs within its nanoconfined channels, thus shortening the reaction distance between L-CDs and ROS and stabilizing their intermediate active species through spatial confinement. This synergistic Zn-MOF/L-CDs composite extended the lifetime of

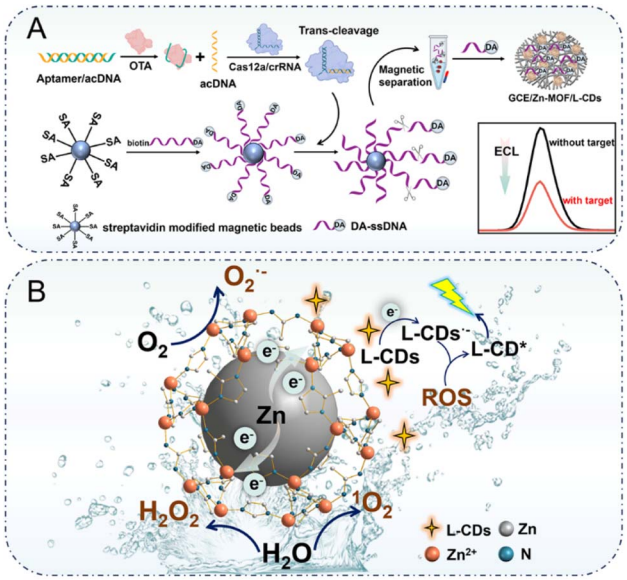

Scheme 1 (A) A diagram of the ECL sensing platform fabrication process. (B) A schematic diagram of the mechanism of self-releasing ROS enhancing ECL based on the MMCT characteristics of Zn-MOF.

ROS and significantly enhanced both the intensity and stability of the luminol ECL signal in aqueous environments. Building on these advancements, a sophisticated analytical platform served as a proof-of-concept model was developed for detecting ochratoxin A (OTA) in complex food matrices. In the presence of OTA, aptamers modified on the surface of Zn-MOF/L-CDs bound to OTA, thereby triggering the release of prehybridized active DNA (acDNA). This activated CRISPR–Cas12a's trans-cleavage activity, which cleaved ssDNA. Then, DA-ssDNA was transferred to the electrode surface following magnetic separation, thereby enabling DA to suppress the initial ECL response (Scheme 1A). Consequently, the synergistic integration of aptamer recognition with trans-cleavage activity of the CRISPR/Cas12a system established a biosensing platform with exceptional sensitivity for trace OTA detection, offering significant potential for applications in food safety monitoring and environmental analysis.

Results and discussion

Structure characterization

To obtain excellent ECL responses from L-CDs, Zn-MOF was synthesized *via* a straightforward one-step solvothermal approach (Fig. 1A) and subsequently used as an efficient co-reaction accelerator. The morphological characteristics of Zn-MOF were elucidated by scanning electron microscopy (SEM). As shown in Fig. 1B, the dense polyhedron was uniformly anchored to the zinc core, thereby forming a hierarchically rough-layered surface that effectively increased surface area and provided a favorable microenvironment for subsequent fixation of the luminescent clusters. Simultaneously, the energy-dispersive spectroscopy (EDS) elemental mapping was utilized to confirm the spatial distribution of constituent elements

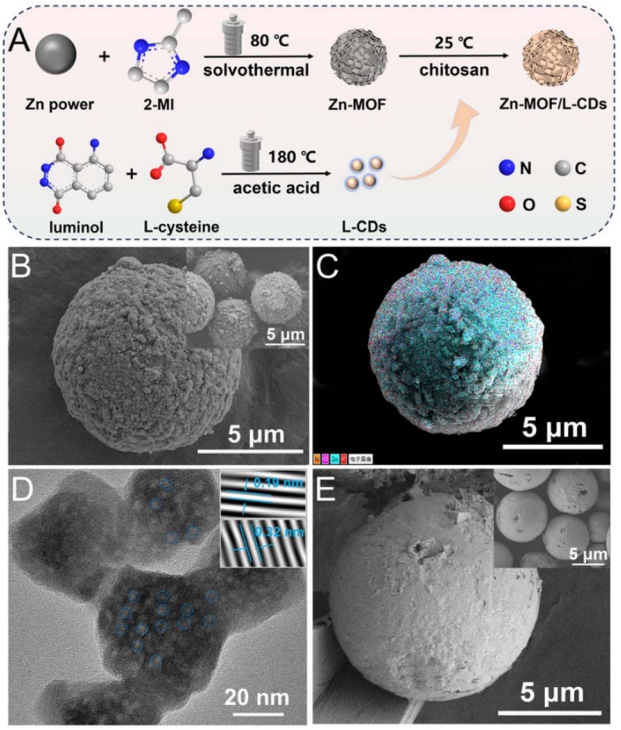

Fig. 1 (A) The synthesis process for L-CDs, Zn-MOF, and Zn-MOF/L-CDs. (B) SEM images and (C) SEM-EDS elemental mapping of Zn-MOF. (D) A HRTEM image of L-CDs. (E) SEM images of Zn-MOF/L-CDs.

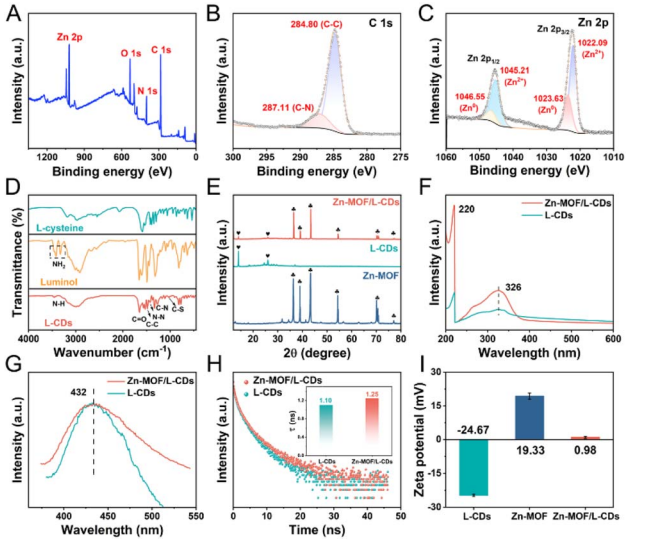

Fig. 2 (A) Zn-MOF, (B) C 1s, and (C) Zn 2p XPS spectra. (D) FT-IR spectra of L-cysteine, luminol, and L-CDs. (E) XRD spectra of Zn-MOF, L-CDs, and Zn-MOF/L-CDs. (F) UV-vis spectra of L-CDs and Zn-MOF/L-CDs. (G) Fluorescence emission spectra of L-CDs and Zn-MOF/L-CDs under an excitation wavelength of 364 nm. (H) TRPL spectra of L-CDs and Zn-MOF/L-CDs. (I) Zeta potential of L-CDs, Zn-MOF, and Zn-MOF/L-CDs.

throughout the Zn-MOF architecture. It could be seen that the Zn core region is predominantly enveloped by a homogeneous shell composed of C, O, and N (Fig. 1C and S1), indicating the successful construction of a Zn-centered coordination network surrounded by organic ligand-derived components. Morphology and lattice of the L-CDs were characterized through high-resolution transmission electron microscopy (HRTEM). As displayed in the blue circle and inset of Fig. 1D, L-CDs exhibited a uniform size distribution and crystalline morphology, as well as obvious lattice fringes, indicating a high degree of crystallinity. The measured lattice spacings of 0.19 and 0.32 nm were assigned to the graphene (100) and graphite (001) planes,[5] respectively. To minimize interference from exogenous reagents, L-CDs were strategically integrated with Zn-MOF to stabilize the luminophore's intermediate active species *via* the framework's confinement, thus significantly enhancing the durability of the ECL signal intensity. As revealed in Fig. 1E, the Zn-MOF/L-CDs composite exhibited greatly reduced surface roughness compared to pristine Zn-MOF. These changes confirmed the successful incorporation of L-CDs, driven by their effective loading and interfacial interactions with the Zn-MOF.

The composition and valence state of elements in Zn-MOF were further investigated by X-ray photoelectron spectroscopy (XPS). Consistent with the EDS results, the XPS survey spectrum revealed peaks for C 1s, N 1s, O 1s, and Zn 2p in Zn-MOF (Fig. 2A), with the C 1s peak used to calibrate the measurements of other elements. As presented in Fig. 2B, two peaks at 284.80 and 287.11 eV were observed in the C 1s spectrum, confirming the existence of C–O and C–N bonds, respectively. The N 1s spectrum showed three chemical states at 398.93, 400.32, and 401.42 eV (Fig. S2A), and they were attributed to C–N=C, N–C, and N–H bonds in 2-methylimidazole, respectively. As depicted in Fig. S2B, the O 1s spectrum was deconvoluted into two peaks at 531.72 (C=O) and 533.02 eV (C–O). The two prominent peaks in the Zn 2p spectrum (Fig. 2C) could be assigned to the Zn $2p_{3/2}$ at 1022.09 eV and the Zn $2p_{1/2}$ hybrid orbitals at 1045.21 eV. Multiplet splitting of the Zn peaks revealed different valence states of Zn^0 and Zn^{2+} in the Zn-MOF.[36] Fourier transform Infrared spectroscopy (FT-IR) spectral analysis of L-cysteine, luminol, and synthesized L-CDs (Fig. 2D) confirmed the structural integrity of key functional groups. The persistence of hydrazide groups (3045 cm^{-1}) in L-CDs provided the basis for ECL emission. Furthermore, peaks for N–H (3416 cm^{-1}), C=O (1649 cm^{-1}), C–C (1475), N–N (1425 cm^{-1}), C–N (1265 cm^{-1}), and C–S (1024 cm^{-1}) in the L-CDs further verified successful S and N heteroatom doping. The formation probably originated from the amination-driven crosslinking during L-CDs synthesis, which preserved the redox-active hydrazide centers while forming graphitic domains with enhanced π-conjugation.[5] X-ray diffraction (XRD) was utilized to examine the crystalline structures of L-CDs, Zn-MOF, and Zn-MOF/L-CDs (Fig. 2E). Notably, in the XRD pattern of L-CDs, there were two distinct peaks at 13° (corresponding to the (002) diffraction peak of graphite) and 25° (attributed to an interplanar structural arrangement identified as the (100) peak). It revealed that Zn-MOF/L-CDs possessed a combination of the lattice structures of Zn-MOF and L-CDs, laying the foundation for the enhanced ECL response.

Moreover, the optical properties of Zn-MOF were analyzed through UV-vis absorption (Fig. 2F) and fluorescence spectroscopy (Fig. 2G). The UV-vis absorption spectra of L-CDs showed two distinct features, a sharp absorption band at 220 nm, likely due to π–π* transitions in the graphitic carbon core, and a characteristic peak at 326 nm, corresponding to *n*–π* transitions of surface-bound hydrazide groups.[37] With the formation of Zn-MOF/L-CDs, the fluorescence emission wavelength remained unchanged, while the emission spectrum broadened. This phenomenon was likely attributed to synergistic interactions among the molecules within the Zn-MOF/L-CDs, which lead to an extended excited-state lifetime.[38,39] To further illustrate the substantial impact of the MMCT effect in Zn-MOF on the excited-state lifetime of L-CDs, time-resolved photoluminescence (TRPL) spectroscopy was employed (Fig. 2H). The average fluorescence lifetime of Zn-MOF/L-CDs (1.25 ns) was longer than that of L-CDs (1.10 ns). It clearly demonstrated that the excited state of the L-CDs could be sustained for an extended period under the confinement effect of Zn-MOF, thereby enhancing the longevity and stability of the ECL signal. Furthermore, as shown in Fig. 2I, the zeta potential of L-CDs was measured to be −24.67 mV, while that of Zn-MOF was 19.33 mV. After cross-linking L-CDs with Zn-MOF, the Zeta potential of the resulting Zn-MOF/L-CDs composites decreased significantly to 0.98 mV. This reduction might be attributed to the successful combination of L-CDs onto the Zn-MOF, which effectively neutralized the Zn-MOF's original surface charge. Collectively, the results confirmed the successful synthesis of Zn-MOF/L-CDs composites and highlighted their enhanced material properties compared to pristine Zn-MOF.

Mechanism of Zn-MOF/L-CDs in boosting the ECL performance

To access Zn-MOF's role as an accelerator in the L-CDs-H_2O/O_2 ECL system, ECL intensities under various conditions were recorded. Fig. 3A showed the ECL intensity–time curves for glass carbon electrodes (GCEs) modified with Zn-MOF (blue curve), luminol (yellow curve), L-CDs (green curve), Zn-MOF + L-CDs (purple curve), and Zn-MOF/L-CDs (red curve). It could be observed that Zn-MOF, luminol, and L-CDs exhibited very low ECL intensities. Although the ECL response of Zn-MOF + L-CDs had been improved, the simple mixing method failed to fully exploit the confinement effect of Zn-MOF. In contrast, the Zn-MOF/L-CDs-modified GCE produced a significantly enhanced ECL signal, indicating that Zn-MOF played a critical role in amplifying the ECL performance of L-CDs rather than serving as a primary luminophore. Simultaneously, the findings were corroborated through electrochemical impedance spectroscopy (EIS) testing (Fig. S3A). Notably, the Zn-MOF/L-CDs composite exhibited a marked reduction in resistance, indicating

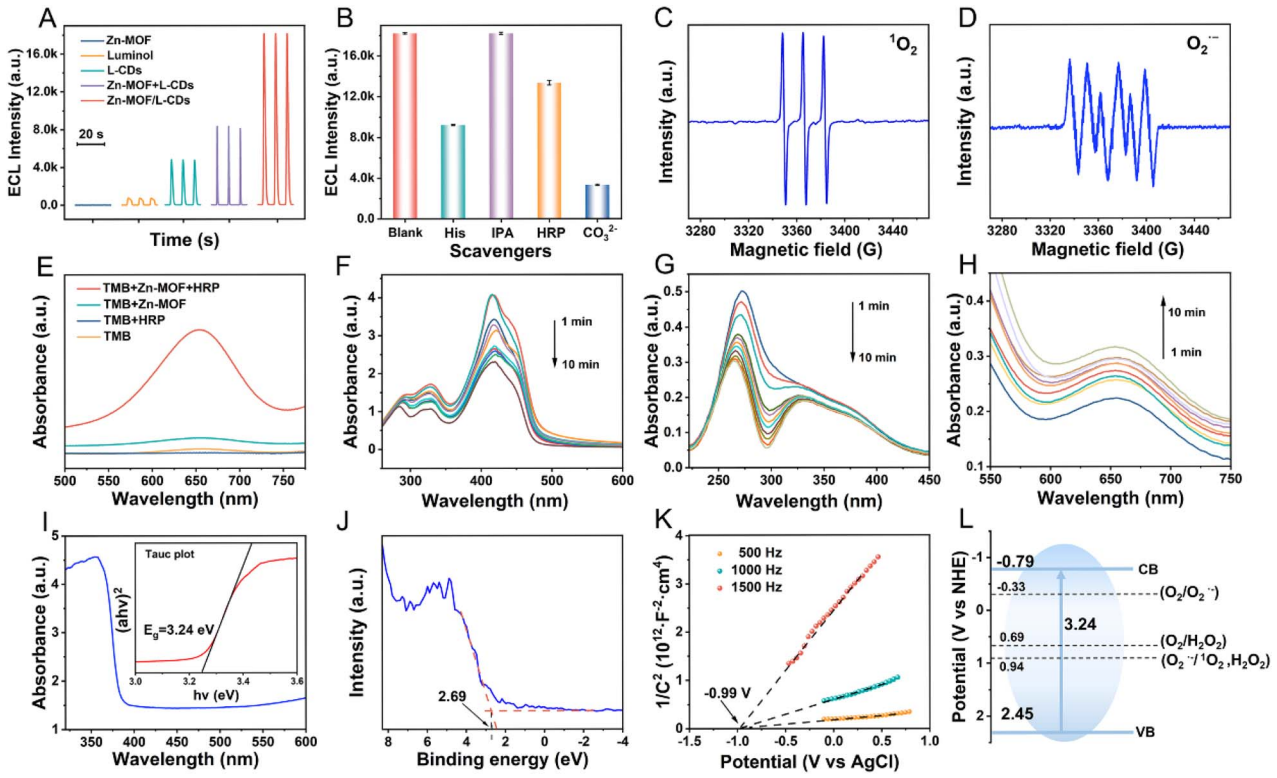

Fig. 3 (A) ECL intensity of Zn-MOF, luminol, L-CDs, Zn-MOF + L-CDs, and Zn-MOF/L-CDs-modified electrodes in 0.1 M PBS (pH 7.4). (B) Effects of blank, 1 mM histidine, 1 mM IPA, 0.4 mg mL^{-1} HRP, and 20 mM CO_3^{2-} radical scavengers on the ECL intensity of Zn-MOF/L-CDs. ESR spectra of (C) $^1O_2$ trapped by TEMP and (D) $O_2^{\cdot-}$ trapped by DMPO. (E) UV-vis absorption spectra of TMB solutions containing different compositions. Time-dependent UV-vis absorption spectra of (F) DPBF (2.0 mg mL^{-1}), (G) NBT (20 μg mL^{-1}), and (H) TMB (20 mM) upon the addition of Zn-MOF (5.0 mg mL^{-1}) from 1 to 10 min. (I) UV-vis DRS and the corresponding Tauc plot curve of Zn-MOF. (J) The VBXPS spectrum and (K) Mott–Schottky plots of Zn-MOF. (L) Band positions of Zn-MOF in relation to the formation potential of ROS.

improved interfacial electron transfer efficiency. This enhancement stemmed from the synergistic combination of Zn-MOF's high porosity and L-CDs' superior conductivity, which facilitated electron transfer, L-CDs oxidation, and ROS generation, aligning with the observed ECL improvement. The cyclic voltammetry (CV) of luminol, L-CDs, and Zn-MOF/L-CDs-modified GCEs all showed oxidation peaks at around 0.6 V compared to Zn-MOF-modified GCE (Fig. S3B). It was demonstrated that the oxidation was due to a reaction with luminol. Specifically, the oxidation peak of Zn-MOF/L-CDs shifted to a lower potential than that of L-CDs alone, indicating that there was a synergistic effect between L-CDs and Zn-MOF, which can significantly accelerate the transport of electrons in the composite system. This effect likely arose from electrons transferred from the zinc core to the MOF shell,[40] facilitating O_2/H_2O reduction and generating abundant ROS to boost L-CDs emission. To further clarify the structural integration of Zn-MOF, N_2 adsorption–desorption measurements were performed (Fig. S4). The results reveal that the Zn-MOF exhibits a Type IV isotherm, indicative of mesopores (5.8 nm), which are sufficiently large to accommodate or surface-anchor L-CDs. The relatively small specific surface area can be attributed to the MOF's thin-layered structure. Besides, to prove the unique role of the Zn-MOF structure in the confinement effect, a pore-free ZnO was successfully synthesized as a direct comparative reference (Fig. S5A and B). Following that, ZnO/L-CDs (Fig. S5C) were prepared using the same mass ratio (5 : 3) as that employed for the optimal Zn-MOF/L-CDs. It can be observed that there is hardly any significant change on the surface of ZnO before and after the composite formation. This may be attributed to ZnO being a non-porous material, and to the small-sized L-CDs being merely adsorbed on its surface. Therefore, owing to the limited interaction between ZnO and L-CDs, the integrated ZnO/L-CDs yields a notably weak ECL signal (Fig. S5D). Therefore, the hierarchical porous architecture of Zn-MOF enhanced the immobilization of L-CDs within its framework while spatially confining ROS diffusion, thereby creating a microenvironment that can effectively improve electron-transfer efficiency and reaction kinetics.

Additionally, the mechanism by which Zn-MOF promotes ECL response was systematically investigated, with a focus on the role of ROS in the simplification pathway. To validate the ROS types involved, targeted radical scavengers were introduced into the ECL system. L-histidine (His),[41] isopropanol (IPA),[42] horseradish peroxidase (HRP), and carbonate (CO_3^{2-})[43] were used as radical scavengers for $^1O_2$, $OH^\bullet$, H_2O_2, and $O_2^{\bullet-}$, respectively. As demonstrated in Fig. 3B, the addition of His, HPR, and CO_3^{2-} significantly quenched ECL intensity compared to the control, whereas no obvious quenching in the ECL intensity was detected after the introduction of IPA. These results indicated that $^1O_2$, H_2O_2, and $O_2^{\bullet-}$ were the primary mediators of ECL amplification in the system. To further confirm the role of ROS in enhancing ECL intensity, electron spin resonance (ESR) spectroscopy was employed without electrical stimulation using 2,2,6,6-tetramethyl-4-piperidine (TEMP) and 5,5-dimethyl-1-pyrroline N-oxide (DMPO) as trapping agents for intermediate radicals. When TEMP was introduced, a characteristic 1 : 1 : 1 triplet signal was observed (Fig. 3C), confirming the generation of $^1O_2$.[44] Similarly, DMPO was used to detect $OH^\bullet$ and $O_2^{\bullet-}$, which typically produce a 1 : 2 : 2 : 1 quartet signal and a strong 1 : 1 : 1 : 1 quartet signal,[45] respectively. In the DMPO-trapped system (Fig. 3D), only the 1 : 1 : 1 : 1 quartet signal corresponding to the DMPO-$O_2^{\bullet-}$ adduct was observed, suggesting the exclusive formation of $O_2^{\bullet-}$ rather than $OH^\bullet$. It was consistent with the test results of IPA as a scavenging agent (Fig. 3B). In addition, the existence of H_2O_2 was further validated using 3,3′,5,5′-tetramethylbenzidin (TMB) as an indicator (Fig. 3E). In the presence of Zn-MOF, TMB was oxidized to its oxidized form, exhibiting a characteristic absorption peak at 652 nm.[46] This oxidation was likely driven by internal electron transfer within the Zn-MOF and its endogenous generation of H_2O_2.[47] Subsequently, the significant increase in absorbance under HRP participation further confirmed the production of H_2O_2. Control experiments with either TMB alone or TMB and HRP showed negligible absorbance, ruling out substrate auto-oxidation or impurity interference. Collectively, these findings provided robust evidence that $^1O_2$, $O_2^{\bullet-}$, and H_2O_2 were critical ROS intermediates in the Zn-MOF/L-CDs-H_2O/O_2 system, driving the observed amplification of ECL intensity. To further verify the ability of Zn-MOF to produce ROS in the absence of electrical stimulation, time-dependent UV-vis spectroscopy analyses were performed to quantify the self-release of $^1O_2$, $O_2^{\bullet-}$, and H_2O_2 by the MMCT effect of Zn-MOF. The concentrations of these species were measured using 1,3-diphenylisobenzofuran (DPBF), 4-nitro blue tetrazolium chloride (NBT), and TMB, respectively. As illustrated in Fig. 3F and G, the oxidation ring-opening reaction between $^1O_2$ and DPBF led to a decrease in absorbance at 420 nm,[48] while the continuous generation of $O_2^{\bullet-}$ resulted in a decrease in absorbance at 259 nm due to its interaction with NBT.[49] This confirmed that Zn-MOF can effectively facilitate the release of $^1O_2$ and $O_2^{\bullet-}$. In contrast, the absorbance of oxidized TMB gradually increased at 652 nm (Fig. 3H), indicating that Zn-MOF continuously promoted the generation of H_2O_2.

To validate Zn-MOF's ability to generate ROS *via* the MMCT effect, the absorption properties and band structures of Zn-MOF were investigated using UV-visible diffuse reflectance spectroscopy (UV-vis DRS), valence band X-ray photoelectron spectroscopy (VBXPS), and Mott–Schottky measurements. As described in Fig. 3I, the UV-vis DRS revealed strong light absorption by Zn-MOF. The band gap energy derived from Tauc plots (Fig. 3F, inset) was 3.24 eV. VBXPS analysis determined the valence band maximum at 2.69 V relative to the Fermi energy (Fig. 3J). Briefly, the valence band maximum *versus* normal hydrogen electrode (NHE) was estimated to be 2.45 V using the formula $E_{NHE}/V = E + \Phi - 4.44$ (E: electrode potential measured by VBXPS; Φ of 4.20 eV: the electron work function of the analyzer).[50] Accordingly, the conduction band (CB) of Zn-MOF was determined as −0.79 V (*vs.* NHE). Simultaneously, the average flat-band positions of Zn-MOF obtained from the Mott–Schottky analyses were −0.99 V (*vs.* Ag/AgCl, −0.79 V *vs.* NHE). Since the bottom of the CB in n-type semiconductors is usually close to the flat band potential,[51] the CB of Zn-MOF was estimated to be −0.79 eV, corroborating the above results (Fig. 3K). Based on these

findings, the band structure of Zn-MOF was constructed (Fig. 3L), providing a theoretical foundation for the generation of $^1O_2$, $O_2^{\bullet-}$, and H_2O_2. Building on the above results, the possible ECL emission mechanism in the Zn-MOF/L-CDs-H_2O/O_2 system, driven by self-releasing ROS, can be described as follows. The clear change in the valence state distribution after reaction could be discerned in Zn 2p XPS spectra (Fig. S7). According to the fitting results, the peak area ratio of Zn^0 to Zn^{2+} decreased from approximately 37% to 28%. Specifically, the XPS peak area for Zn^0 significantly decreased post-reaction, while the peak area for Zn^{2+} correspondingly increased, indicating partial oxidation of Zn^0 to Zn^{2+} occurred during the reaction. The electron–transfer processes outlined in eqn (1) and (2) facilitated the reduction of H_2O and dissolved O_2 into ROS, specifically $O_2^{\bullet-}$, $^1O_2$, and H_2O_2, as described in eqn (3)–(5). Concurrently, L-CDs were electrochemically oxidized to form the radical cation L-CDs$^{\bullet+}$ (eqn (6)). This species reacted with ROS to produce the excited-state L-CDs* (eqn (7)), which subsequently relaxed to its ground state, emitting light as shown in eqn (8) and depicted in Scheme 1B.

Self-releasing ROS:

$$Zn - e^- \rightarrow Zn^+ \quad (1)$$

$$Zn^+ - e^- \rightarrow Zn^{2+} \quad (2)$$

$$O_2 + e^- \rightarrow O_2^{\bullet-} \quad (3)$$

$$2O_2^{\bullet-} + 2H^+ \rightarrow {}^1O_2 + H_2O_2 \quad (4)$$

$$O_2 + 2H^+ + 2e^- \rightarrow H_2O_2 \quad (5)$$

ECL emission:

$$L\text{-}CDs - e^- \rightarrow L\text{-}CDs^+ \quad (6)$$

$$L\text{-}CDs^+ + O_2^{\bullet-}/{}^1O_2/H_2O_2 \rightarrow L\text{-}CDs^* + \text{products} \quad (7)$$

$$L\text{-}CDs^* \rightarrow L\text{-}CDs + hv \quad (8)$$

Furthermore, density functional theory (DFT) calculations were employed to elucidate the mechanism underlying the self-release of ROS *via* the MMCT effect of the Zn-MOF, thereby enhancing the ECL response of L-CDs. The optimized structural configuration of Zn-MOF (Fig. 4A) was simulated by DFT in conjunction with the crystal structure of the zeolitic imidazolate frameworks model. In this structure, the Zn core is coordinated to nitrogen atoms in the MOF shell, facilitating continuous electron injection into the MOF shell *via* MMCT. The charge density difference plot at the Zn core-MOF shell interface (Fig. 4B) provided clear insight into the charge distribution, confirming a strong interaction and significant charge transfer from Zn core to MOF shell. Similarly, the charge density difference plot for O_2–Zn-MOF (Fig. 4C) revealed pronounced charge accumulation in the region occupied by O_2, offering compelling evidence for the transformation of oxygen molecules into $O_2^{\bullet-}$. In addition, the types of ROS released spontaneously from Zn-MOF were explored to assess potential reaction pathways and identify rate-determining steps (RDSs). In the presence of H_2O and O_2, the ROS formation pathway followed OO* → OOH* → H_2O_2 + $^1O_2$, with a negative free energy for the RDS (OO* → OOH*), indicating a spontaneous reaction (Fig. 4D). Therefore, self-releasing ROS, including $O_2^{\bullet-}$, H_2O_2, and $^1O_2$, can be realized based on the MMCT effect of Zn-MOF under neutral conditions. Given the high propensity of H_2O_2 to decompose, two potential decomposition pathways were simulated to assess the likelihood of OH$^{\bullet}$ formation (Fig. 4E and F). Both pathways exhibited positive free energies for their respective RDSs (2OH* → OOH* and O* → OOH*), suggesting that OH$^{\bullet}$ generation was thermodynamically unfavorable. The

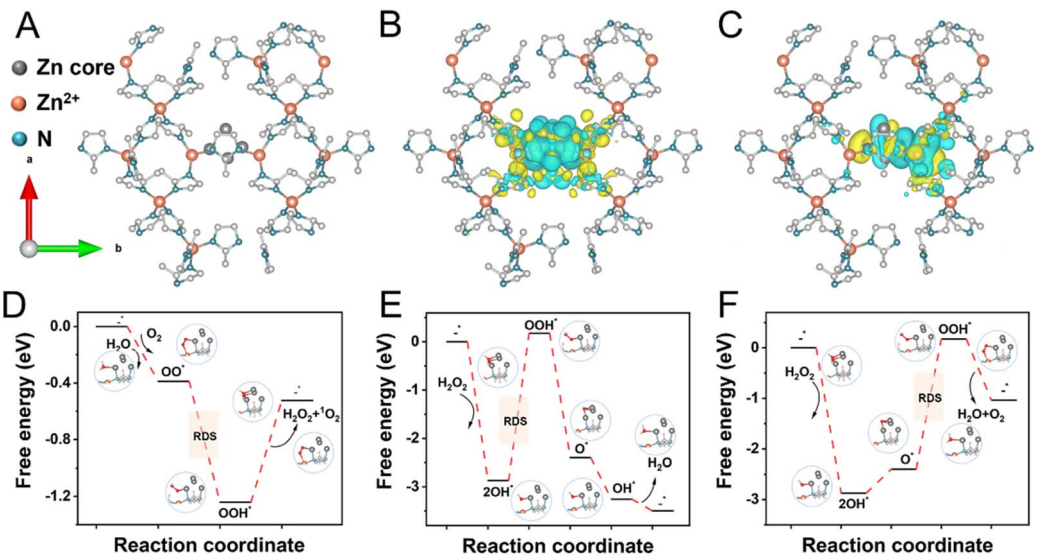

Fig. 4 (A) The optimized structural configuration of Zn-MOF. Charge density difference plots of (B) Zn-MOF and (C) O_2–Zn-MOF. Yellow: charge accumulation; cyan: charge depletion. DFT-derived free energy diagrams for (D) potential reaction pathways of ROS and (E, F) two potential H_2O_2 decomposition pathways.

above results clearly showed that the self-release of $O_2^{\bullet -}$, H_2O_2, and $^1O_2$ can be achieved by the MMCT effect of Zn-MOF. This theoretical derivation was highly consistent with the experimental observations, providing a reasonable explanation for the phenomena and further validating the charge transfer mechanism and the product-formation characteristics of Zn-MOF in the related reaction process.

Feasibility and analytical performance of the ECL sensing platform

To validate the efficient trans-cleavage activity of the CRISPR/Cas12a system, a 20% polyacrylamide gel electrophoresis (PAGE) assay was performed. As illustrated in Fig. 5A, lane 3 (aptamer + acDNA) exhibited a distinct electrophoretic mobility shift compared to lanes 1 (aptamer) and 2 (acDNA), confirming the formation of a double-stranded DNA (dsDNA) hybridized structure. Notably, lane 4 demonstrated the selective displacement of acDNA from the dsDNA hybrid upon introduction of OTA, as evidenced by the reappearance of acDNA bands at positions corresponding to their monomeric forms. This observation confirmed the high-affinity binding of OTA to the aptamer, triggering a conformational change to release acDNA. Lanes 5 (crRNA) and 6 (ssDNA) as critical controls confirmed the absence of non-specific interactions in the absence of active Cas12a. Critically, the acDNA liberated from the OTA-triggered dissociation was subsequently employed as a catalytic trigger to activate the crRNA/Cas12a ribonucleoprotein complex. The trans-cleavage activity of the activated Cas12a was unequivocally validated in lanes 7–9, where the slightly dimmer of the ssDNA substrate band (lane 9) than that in lane 6 strictly depended on the simultaneous presence of Cas12a, crRNA, and acDNA, confirming the functional integrity in the biosensing platform. Furthermore, the characteristics of the sensing interface were meticulously scrutinized using EIS during the assembly process. As exhibited in Fig. S8, compared with GCE, the resistance value of Zn-MOF/L-CDs was significantly increased. The observed phenomenon could be ascribed to the poor conductivity of the Zn-MOF, which enhanced the interfacial resistance. The subsequent addition of DA-ssDNA further increased resistance, reflecting reduced conductivity at the electrode interface.

Under optimized experimental conditions (Fig. S9A–C), the ECL sensing platform's sensitivity and quantitative detection range were rigorously evaluated by incubating it with OTA at varying concentrations. As illustrated in Fig. 5B, upon incubation with OTA across a broad concentration range from 10^{-5} to 10^3 ng mL^{-1}, a progressive attenuation of the ECL signal was observed. Fig. 5C displayed that the change in ECL intensity (ΔI_{ECL}) was logarithmically proportional to OTA concentration, with a linear regression equation of $\Delta I_{ECL} = 11\,079 + 1570\lg c$ and a correlation coefficient of $R^2 = 0.9934$. Remarkably, the detection limit achieved in this study was as low as 0.13 fg mL^{-1} (S/N = 3), offering a significantly lower detection limit and a wider linear range than in previous studies, as summarized in Table S1. The enhanced performance stems from the synergistic interplay between the MMCT mechanism and the confinement effect in Zn-MOF, which boosts the efficiency of ROS generation and stabilizes the luminol-derived intermediate active species. Besides, the high affinity between the aptamer and OTA ensures precise target recognition and efficient signal transduction.

Additionally, the stability of the ECL sensing platform was evaluated as a key indicator of its practical utility. As shown in Fig. 5D, there was no significant fluctuation in the ECL intensity during a 500 s potentiometric scan, with a relative standard deviation (RSD) of 1.18%, demonstrating excellent operational

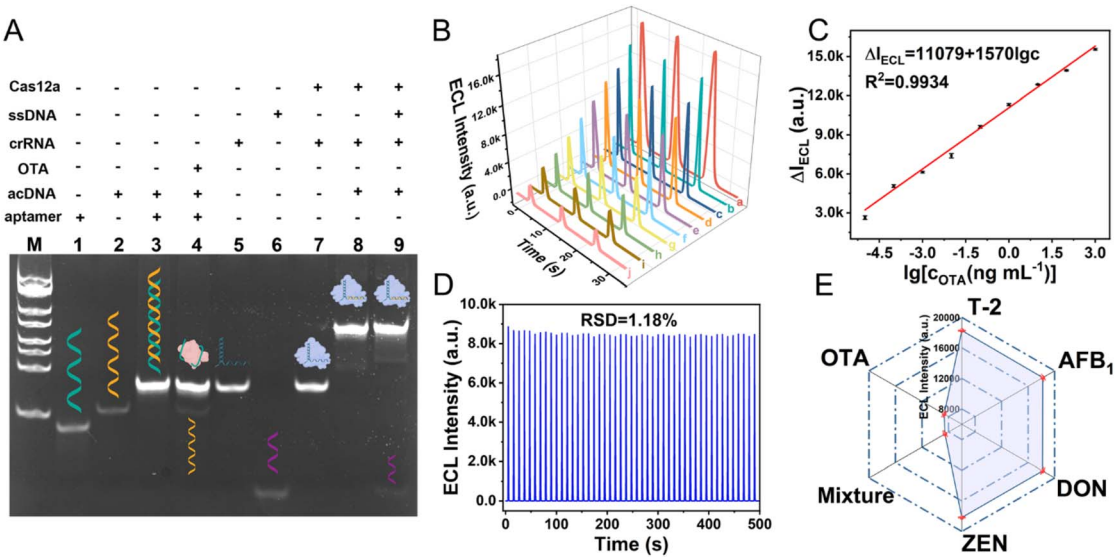

Fig. 5 (A) PAGE analysis verified the high efficiency trans-cleavage ability of CRISPR/Cas12a toward ssDNA. (B) ECL curves with different concentrations of OTA (a–j: 0, 0.00001, 0.0001, 0.001, 0.01, 0.1, 1, 10, 100, and 1000 ng mL^{-1}) and (C) the corresponding calibration plot. (D) Cycling stability and (E) selectivity of the sensing platform with 0.1 ng mL^{-1} OTA in 0.1 M PBS (pH 7.4). Error bars in all graphs represent standard deviations in triplicate experiments.

reliability. The significant stability is attributed to the MMCT effect of the Zn-MOF, which allows Zn^0 to be continuously oxidized to Zn^{2+} over multiple cycles, providing a stable source of ROS. At the same time, the MMCT effect of Zn-MOF effectively prevents electrode contamination and maintains consistent electron-transfer kinetics at the interface under repeated electrochemical stimulation. What's more, the proposed ECL biosensor demonstrated robust long-term stability after 30 days of storage at 4 °C (Fig. S10), confirming its suitability for real-time, deployable analytical applications. To evaluate the specificity of the ECL sensing platform under environmentally relevant conditions, interference studies were conducted using 0.1 ng mL^{-1} OTA alongside 10-fold higher concentrations of co-occurring mycotoxins, including aflatoxin B_1 (AFB_1), T-2 toxin (T-2), deoxynivalenol (DON), and zearalenone (ZEN). As evidenced by the ECL response profiles in Fig. 5E, the quenching effects induced by interfering species were statistically negligible, whereas significant signal suppression was exclusively observed for OTA and its mixtures. The remarkable selectivity is attributed to the aptamer's strong affinity for OTA, demonstrating the platform's distinctive specificity. To evaluate practical applicability in complex environmental matrices, OTA recovery experiments were performed in corn and peanut samples using the standard addition method (pretreatment details in SI Materials). The platform exhibited exceptional accuracy and reproducibility, achieving recoveries of 98.72–101.6% across triplicate measurements with RSD below 2.29%, as detailed in Table S2, confirming its robustness for real-sample analysis.

Conclusions

In summary, a highly sensitive and selective biosensing platform was developed by leveraging the synergistic enhancement of the MMCT effect and the Zn-MOF confinement effect, enabling the robust detection of OTA in complex matrices. The MMCT effect in Zn-MOF facilitated continuous endogenous ROS release in the Zn-MOF/L-CDs-H_2O/O_2 system, eliminating reliance on traditional exogenous oxidants and simplifying the sensing system design. By integrating L-CDs with Zn-MOF, the intensity and stability of ECL signals in the neutral environment were significantly improved. Confinement effect-mediated Zn-MOF shortens the reaction distance between L-CDs with ROS and stabilizes the luminescent intermediates. The high affinity between OTA and its aptamers facilitated the release of acDNA. Then, in turn, the CRISPR–Cas12a system was activated to cleave ssDNA, enabling precise regulation of the interfacial electron-transfer process. This synergy between the MMCT and confinement effects establishes a novel approach for constructing ECL biosensors, offering significant potential for the sensitive and accurate detection of mycotoxins in food and environmental samples.

Author contributions

X. M. conducted most of the experiments in the project, including data curation, formal analysis, and writing the original draft of the manuscript. M. Y. and J. Y. provided extensive resource support, supplying essential experimental equipment and research materials critical to the research. S. Z., J. Z., and Y. Z. jointly took charge of conceiving and supervising the research, funding acquisition, managing project administration, and critically revising the manuscript to ensure scholarly rigor.

Conflicts of interest

There are no conflicts of interest to declare.

Data availability

The data supporting this article have been included as part of the Supplementary Information (SI). Supplementary information: detailed descriptions of the experimental processes, supporting figures, and supporting tables. See DOI: https://doi.org/10.1039/d5sc09465h.

Acknowledgements

This work was financially supported by the National Natural Science Foundation of China (52173168), the Taishan Scholars Program (tsqn202103082), the Shandong Provincial Natural Science Foundation (ZR2025MS267), the Excellent Youth Innovation Team in Universities of Shandong (2021KJ021), and the Science and Technology Program of the University of Jinan (XKY2203, XBS2419). The authors would like to thank Scientific Compass (https://www.shiyanjia.com) for supporting XPS and Zeta potential tests.

References

1 Y. Shi and Y. Liu, Qualitative and quantitative electrochemiluminescence evaluation of trace Pt single-atom in MXenes, *Nat. Commun.*, 2024, **15**, 7086.
2 M. Xi, Z. Wu, Z. Luo, L. Ling, W. Xu, R. Xiao, H. Wang, Q. Fang, L. Hu, W. Gu and C. Zhu, Water activation for boosting electrochemiluminescence, *Angew. Chem., Int. Ed.*, 2023, **62**, e202302166.
3 M. Liu, M. Liu, W. Chen, F. Li, S. Cai, S.-J. Lin, X. Chen and Z. Cai, Identifying N coordination types of single-atom catalysts by spin-modulated luminol cathodic electrochemiluminescence, *Angew. Chem., Int. Ed.*, 2024, **64**, e202421755.
4 T. Xiang, J. Wang, Y. Liang, W. Daoudi, W. Dong, R. Li, X. Chen, S. Liu, S. Zheng and K. Zhang, Carbon dots for anti-corrosion, *Adv. Funct. Mater.*, 2024, **34**, 2411456.
5 L. Wang, W.-J. Zeng, X. Yang, R. Yuan, W.-B. Liang and Y. Zhuo, Engineering molecular emission centers of carbon dots to boost the electrochemiluminescence for the detection of cancer cells, *Anal. Chem.*, 2023, **95**, 13897–13903.
6 S. Kiani Shahvandi, M. Ghaedi and H. Ahmar, A New Approach for the determination of metronidazole using switchable solvent coupled with Au-MWCNTs-modified electrochemical sensor, *J. Anal. Test.*, 2024, **8**, 191–200.

7 X. Zhang, W. Wang, L. Guan, H. Chen, D. Li, L. Zhang and S. Huang, Preparation of a novel green fluorescent carbon quantum dots and application in Fe^{3+}-specific detection in biological system, *J. Anal. Test.*, 2024, **8**, 40–51.

8 H. Gao, T. Sun, W. Wang, J. Li, M. Zhang, Y. Hou and G. Bai, Self-illuminating copper-luminol coordination polymers for bioluminescence imaging of oxidative damage, *Anal. Chem.*, 2024, **96**, 16434–16442.

9 C. Ding, Y. Li, L. Wang and X. Luo, Ratiometric electrogenerated chemiluminescence cytosensor based on conducting polymer hydrogel loaded with internal standard molecules, *Anal. Chem.*, 2019, **91**, 983–989.

10 H. Liu, S. Jiang, M. Li, S. Lei, J. Wu, T. He, D. Wang, J. Lin and P. Huang, Dual enzyme-driven cascade reactions modulate immunosuppressive tumor microenvironment for catalytic therapy and immune activation, *ACS Nano*, 2024, **18**, 30345–30359.

11 M. Lin, X. Lv, H. Wang, L. Shu, H. Wang, G. Zhang, J. Sun and X. Chen, Coacervation-driven semipermeable nanoreactors for enzymatic cascade-mediated cancer combination therapy with enhanced efficacy, *Adv. Mater.*, 2024, **36**, 2407378.

12 L.-B. Zhu and S.-N. Ding, Coreactant-free electrochemiluminescence: ROS generation *via* upconversion nanoparticles-sensitized inverse opal TiO_2 photocatalysis under NIR irradiation, *Anal. Chem.*, 2025, **97**, 7546–7554.

13 W. Liu, R. Shao, L. Guo, J. Man, C. Zhang, L. Li, H. Wang, B. Wang, L. Guo, S. Ma, B. Zhang, H. Diao, Y. Qin and L. Yan, Precise design of TiO_2@CoO_x heterostructure *via* atomic layer deposition for synergistic sono-chemodynamic oncotherapy, *Adv. Sci.*, 2024, **11**, 2304046.

14 E. Ju, K. Dong, Z. Chen, Z. Liu, C. Liu, Y. Huang, Z. Wang, F. Pu, J. Ren and X. Qu, Copper(II)–graphitic carbon nitride triggered synergy: improved ROS generation and reduced glutathione levels for enhanced photodynamic therapy, *Angew. Chem., Int. Ed.*, 2016, **55**, 11467–11471.

15 G. Feng, H. Huang, M. Zhang, Z. Wu, D. Sun, Q. Chen, D. Yang, Y. Zheng, Y. Chen and X. Jing, Single atom iron-doped graphic-phase C_3N_4 semiconductor nanosheets for augmented sonodynamic melanoma therapy synergy with endowed chemodynamic effect, *Adv. Sci.*, 2023, **10**, 2302579.

16 X. Liang, M. Chen, P. Bhattarai, S. Hameed, Y. Tang and Z. Dai, Complementing cancer photodynamic therapy with ferroptosis through iron oxide loaded porphyrin-grafted lipid nanoparticles, *ACS Nano*, 2021, **15**, 20164–20180.

17 W. You, Z. Cai, F. Xiao, J. Zhao, G. Wang, W. Wang, Z. Chen, W. Hu, Y. Chen and Z. Wang, Biomolecular microneedle initiates Fe_3O_4/MXene heterojunction-mediated nanozyme-like reactions and bacterial ferroptosis to repair diabetic wounds, *Adv. Sci.*, 2025, **12**, 2417314.

18 H. Xie, L. Zhang, J. Chen, C. Wang, Y. Yan, S. Deng, K. Liu, D. Li, M. Yang, J. Ren, S. Wu and Y. Han, A dual-catalysis mode for ROS regulation to accelerate biointegration of implants in infected diabetic wound, *Adv. Funct. Mater.*, 2025, **35**, 2423015.

19 X. Zhou, Q. Zhou, Z. He, Y. Xiao, Y. Liu, Z. Huang, Y. Sun, J. Wang, Z. Zhao, X. Liu, B. Zhou, L. Ren, Y. Sun, Z. Chen and X. Zhang, ROS balance autoregulating core–shell CeO_2@ZIF-8/Au nanoplatform for wound repair, *Nano-Micro Lett.*, 2024, **16**, 156.

20 X. Zhang, J. Ma, S. Zhou, H. Yang, J. Yu and Y. Zhang, Organic frameworks-based electrochemiluminescence sensors for point-of-care testing, *Coord. Chem. Rev.*, 2026, **546**, 217098.

21 J. Zhuang, S. Liu, B. Li, Z. Li, C. Wu, D. Xu, W. Pan, Z. Li, X. Liu and B. Liu, Electron transfer mediator modulates type II porphyrin-based metal–organic framework photosensitizers for type I photodynamic therapy, *Angew. Chem., Int. Ed.*, 2025, **64**, e202420643.

22 D. W. Kang, J. H. Kim, J. H. Lim, Y. Kim, M. Kang, J. Shin, S. Son, H. Yun, H. Kim, S. Park, J. Y. Lee, J. S. Kim and C. S. Hong, Promoted type I and II ROS generation by a covalent organic framework through sonosensitization and PMS activation, *ACS Catal.*, 2022, **12**, 9621–9628.

23 L. Xu, X. Mei, S. Zhou, J. Zhang, P. Zhu, J. Yu and Y. Zhang, Active Radicals Enriched by the Nanoconfinement Effect Synergistically Enhance Electrochemiluminescence with a Co-Reaction Accelerator for Zearalenone Detection, *Anal. Chem.*, 2025, **97**, 21508–21517.

24 J. Huang, G. Deng, S. Wang, T. Zhao, Q. Chen, Y. Yang, Y. Yang, J. Zhang, Y. Nan, Z. Liu, K. Cao, Q. Huang and K. Ai, A NIR-II photoactivatable "ROS Bomb" with high-density Cu_2O-supported MoS_2 nanoflowers for anticancer therapy, *Adv. Sci.*, 2023, **10**, 2302208.

25 X.-W. Gao, Z.-W. Zhao, Y. He, S.-F. Fan, K.-R. Jiao, S.-Y. Lou, X.-Y. Han, P.-F. Song, R. Cai, Z. Hu, Z.-J. Jiang, Y.-J. Wang and J.-Q. Zhu, Nanodiamond: a promising metal-free nanoscale material in photocatalysis and electrocatalysis, *Rare Met*, 2024, **43**, 3501–3552.

26 W. Li, J. Tu, J. Sun, Y. Zhang, J. Fang, M. Wang, X. Liu, Z.-Q. Tian and F. Ru Fan, Boosting reactive oxygen species generation *via* contact-electro-catalysis with Fe^{III}-initiated self-cycled fenton system, *Angew. Chem., Int. Ed.*, 2025, **64**, e202413246.

27 Y. Yuan, X. Xi, T. Bao, P. Bian, F. Pei, X. Zhang, S. Wang and W. Wen, Integrating Bimetallic Nanoparticles with Covalent Organic Frameworks as Multifunctional Nanozyme for Colorimetric Detection of Hydrogen Peroxide and Glutathione, *J. Anal. Test.*, 2024, **8**, 278–287.

28 X. Y. Gong, L. Z. Su, S. Y. Peng, Y. Xia, J. J. Guo, L. B. Zou, B. X. Fu, F. Huang, J. F. Liu and C. H. Yang, A pH-responsive cascade nano-reactor elevates ROS generation by remodeling biofilm microenvironment for enhanced antibacterial treatment, *Adv. Funct. Mater.*, 2025, **35**, 2425467.

29 N. Gao, G. Ren, M. Zhang and L. Mao, Electroless deposition of palladium nanoparticles on graphdiyne boosts electrochemiluminescence, *J. Am. Chem. Soc.*, 2024, **146**, 3836–3843.

30 F.-Y. Ren, C. Hu, W.-B. Huang, L.-H. Duan, Y.-Z. Meng, X.-L. Li, Z. Fang, X.-Y. Zhao, W. Wang, X.-S. Li, J. Zhao, X.-Y. Zhang, S.-L. Hou, H. Xu, Y. Shi, L.-N. He and B. Zhao,

Modulated multicomponent reaction pathway by pore-confinement effect in MOFs for highly efficient catalysis of low-concentration CO_2, *Angew. Chem., Int. Ed.*, 2025, **64**, e202503898.

31 Y. Bing, Z. Song, H. Jiang, X. Xu, Z. Yu, T. Zhou and T. Zhang, A"Duet-Insurance" sensing strategy by combining Janus TpMa COF/Eu-doped α-Fe_2O_3 and variable-temperature excitation for robust, visual indoor pollution gas detection, *Adv. Funct. Mater.*, 2025, **35**, 2417599.

32 P. Scrimin and L. J. Prins, Sensing through signal amplification, *Chem. Soc. Rev.*, 2011, **40**, 4488–4505.

33 Z. Zhao, R. Wang, X. Yang, J. Jia, Q. Zhang, S. Ye, S. Man and L. Ma, Machine learning-assisted, dual-channel CRISPR/Cas12a biosensor-in-microdroplet for amplification-free nucleic acid detection for food authenticity testing, *ACS Nano*, 2024, **18**, 33505–33519.

34 X. Zhong, L. Luo, J. Wu, W. Li, X. Liu, T. Ye, Z. Li and P. Shi, Adhesion-assisted antioxidant-engineered Mesenchymal stromal cells for enhanced cardiac repair in myocardial infarction, *ACS Nano*, 2025, **19**, 11412–11426.

35 X. Bao, J. Zhao, J. Sun, M. Hu and X. Yang, Polydopamine nanoparticles as efficient scavengers for reactive oxygen species in periodontal disease, *ACS Nano*, 2018, **12**, 8882–8892.

36 W. Wen, Y. Lang, Z. Li, L. Li, H.-W. Li, Y. Li and G. Wen, A Fe/Zn dual single-atom nanozyme with high peroxidase activities for detection of penicillin G, *Anal. Chem.*, 2024, **96**, 19248–19257.

37 K. Ji, S. Xia, X. Sang, A. M. Zeid, A. Hussain, J. Li and G. Xu, Enhanced luminol chemiluminescence with oxidase-like properties of FeOOH nanorods for the sensitive detection of uric acid, *Anal. Chem.*, 2023, **95**, 3267–3273.

38 D. Kim and T. S. Teets, Sterically encumbered aryl isocyanides extend excited-state lifetimes and improve the photocatalytic performance of three-coordinate Copper(I) β-Diketiminate charge-transfer chromophores, *J. Am. Chem. Soc.*, 2024, **146**, 16848–16855.

39 Y. Wang, X. Wang, Z. Liu, F. Dong and Y. Lin, Ce-MOFs Fluorescent Probes with Different Ligands for Phosphate Detection, *J. Anal. Test.*, 2024, **8**, 431–440.

40 J. Wang, S. P. Teong, S. N. Riduan, A. Armugam, H. Lu, S. Gao, Y. K. Yean, J. Y. Ying and Y. Zhang, Redox active Zn@MOFs as spontaneous reactive oxygen species releasing antimicrobials, *J. Am. Chem. Soc.*, 2024, **146**, 599–608.

41 Y. Peng, L. Yu, M. Sheng, Q. Wang, Z. Jin, J. Huang and X. Yang, Room-temperature synthesized iron/cobalt metal–organic framework nanosheets with highly efficient catalytic activity toward luminol chemiluminescence reaction, *Anal. Chem.*, 2023, **95**, 18436–18442.

42 H. Wu, H. Sun, R. A. J. F. Oerlemans, S. Li, J. Shao, J. Wang, R. R. M. Joosten, X. Lou, Y. Luo, H. Zheng, L. K. E. A. Abdelmohsen, H. H. P. Garza, J. C. M. van Hest and H. Friedrich, Understanding, mimicking, and mitigating radiolytic damage to polymers in liquid phase transmission electron microscopy, *Adv. Mater.*, 2024, **36**, 2402987.

43 Z. Luo, W. Xu, Z. Wu, L. Jiao, X. Luo, M. Xi, R. Su, L. Hu, W. Gu and C. Zhu, Iron single-atom catalyst-enabled peroxydisulfate activation enhances cathodic electrochemiluminescence of Tris(bipyridine) ruthenium(II), *Anal. Chem.*, 2023, **95**, 10762–10768.

44 D. Kong, Y. Fan, F. Wang, F. Zhang, Q. Zhao, Z. Sun, J. Yao, M. Chu, G. Wang, G. Zhang, Z. Guan, H. Sheng and Y. Wang, Boosting singlet oxygen oxidation of micropollutants at an enzyme-like bifunctional single-atom catalyst interface, *ACS Catal.*, 2025, **15**, 8174–8184.

45 J.-H. Li, J.-L. Liu, X.-L. Zhang, X.-C. Zhu, R. Yuan and Y.-Q. Chai, Ultrasensitive electrochemiluminescence biosensor based on 2D Co_3O_4 nanosheets as a coreaction accelerator and highly ordered rolling DNA nanomachine as a signal amplifier for the detection of microRNA, *Anal. Chem.*, 2023, **95**, 4131–4137.

46 H. Cao, Y. Lu, X. Zhang, W. Dong, W. Shi and Y. Huang, Engineering a simple multisignal-output probe for measuring residual peroxymonosulfate in advanced oxidation reactions, *Chem. Eng. J.*, 2023, **471**, 144663.

47 H. Sun, Y. Gao, N. Hu, Y. Zhang, C. Guo, G. Gao, Z. Ma, K. Ivan Ivanovich and Y. Qiu, Electronic coupling between molybdenum disulfide and gold nanoparticles to enhance the peroxidase activity for the colorimetric immunoassays of hydrogen peroxide and cancer cells, *J. Colloid Interface Sci.*, 2020, **578**, 366–378.

48 H.-P. Zhang, Q. Yi, X.-Y. Guan, R.-R. Dai, J. Pang, Q. Zhong, S. Tan, D. Luo, Y. Y. Li, M. Xie, X.-P. Zhou and D. Li, Metal-organic frameworks enable spontaneous singlet oxygen generation without light irradiation, *Angew. Chem., Int. Ed.*, 2025, **64**, e202507349.

49 C. Hu, H. Huang, F. Chen, Y. Zhang, H. Yu and T. Ma, Coupling piezocatalysis and photocatalysis in Bi_4NbO_8X (X = Cl, Br) polar single crystals, *Adv. Funct. Mater.*, 2020, **30**, 1908168.

50 Q. Liao, Q. Sun, H. Xu, Y. Wang, Y. Xu, Z. Li, J. Hu, D. Wang, H. Li and K. Xi, Regulating relative nitrogen locations of diazine functionalized covalent organic frameworks for overall H_2O_2 photosynthesis, *Angew. Chem., Int. Ed.*, 2023, **62**, e202310556.

51 M.-Y. Yang, S.-B. Zhang, M. Zhang, Z.-H. Li, Y.-F. Liu, X. Liao, M. Lu, S.-L. Li and Y.-Q. Lan, Three-Motif molecular junction type covalent organic frameworks for efficient photocatalytic aerobic oxidation, *J. Am. Chem. Soc.*, 2024, **146**, 3396–3404.

